ADVANCED ELECTRONIC MATERIALS
www.advelectronicmat.de

Ultrabroadband Photodetector Based on Ferromagnetic van der Waals Heterodiode

Xin Hu, Jie Hou, Qingsong Dong, Zhiyi Liu, Suofu Wang, Fang Wang, Yubing Tu, Tao Han, Feng Li, Zongyuan Zhang, Xingyuan Hou, Shaoliang Wang, Dongxu Zhao, Lei Shan,* and Mingsheng Long**

The discovery of 2D ferromagnetic (FM) van der Waals (vdW) semiconductors with narrow bandgap and *p*-type transport behavior makes them promising for infrared photodetection. Here, a 2D vdW heterodiode uncooled long-wave infrared (LWIR) photodetector by stacking a *p*-type 2D FM material $CrSiTe_3$ on top of an *n*-type transition metal dichalcogenides (TMDs) MoS_2 is reported. A good rectification ratio $>10^2$ and an ultra-broadband photoresponse from 0.52 to 10.6 μm are demonstrated. The photoresponsivity of up to 20.7 A W^{-1} and the external quantum efficiency (EQE) of up to 4031.7% are obtained under a 1310 nm laser at a −1 V bias in ambient, which indicates that these $CrSiTe_3$–MoS_2 p–n junction devices have a good photovoltaic response. Meanwhile, the photovoltaic responsivity up to 0.15 A W^{-1}, EQE up to 29.7%, and fast response with a decay time of 2.8 μs at 637 nm are demonstrated. In addition, the room temperature mid-wave infrared (MWIR) specific detectivity and LWIR specific detectivity of $CrSiTe_3$–MoS_2 is 6.1×10^9 cm $Hz^{1/2}$ W^{-1} and 1.93×10^9 cm $Hz^{1/2}$ W^{-1}, respectively. These observations open up possibilities for developing high-sensitive infrared detection based on the valley optical selection rule and LWIR image technology.

1. Introduction

The recent discovery of 2D ferromagnetic (FM) materials including CrI_3,[1] $CrGeTe_3$,[2] and Fe_3GeTe_2[3] could be down to the monolayer with intrinsic ferromagnetic, which offers a platform to explore fundamental physics and smart functional devices. The physical properties of 2D layered magnetism are more susceptible to external stimuli, such as gate voltage,[4–6] current injection,[7] electrostatic doping,[8–10] pressure,[11,12] and strain.[13] In particular, the intrinsic 2D FM semiconductors have attracted great interest since both ferromagnetism and semiconducting properties are ideal for next-generation magnetoelectric and magneto-optical applications. The family of $CrXTe_3$ (X = Si, Ge, Sn) belongs to this category, the optical bandgap is ≈0.4 eV for $CrSiTe_3$[14,15] ≈0.7 eV for $CrGeTe_3$[16] and ≈0.9–1.2 eV for $CrSnTe_3$.[17] Fortunately, good electronic contacts between the $CrSiTe_3$ and metal electrodes could be realized when the thickness of the $CrSiTe_3$ flakes is >7 nm.[15] The $CrSiTe_3$, *p*-type semiconducting transport behavior in combination with the narrow bandgap 2D ferromagnetism has great potential application in mid-wave infrared (MWIR) photodetection. Integratable, room temperature operation MWIR, and long-wave infrared (LWIR) photodetectors are highly desired for the wide application in many important fields such as thermal image, infrared guiding, molecular "fingerprint" identification, free space telecommunication.[18,19] To date, broadband photodetection based on $CrSiTe_3$ remain elusive. To realize high-performance uncooled LWIR photodetection, the current noise power density and dark current should be well suppressed. The widely used strategy of suppressing current noise and dark current in 2D materials-based photodetectors is inducing a built-in electrical field. Here, we report a highly-sensitive uncooled MWIR and LWIR photodetector by stacking a *p*-type 2D FM $CrSiTe_3$ on top of *n*-type 2D layered materials such as MoS_2. The *n*-type MoS_2 is a good absorber in the visible and near-infrared range, which was used to enhance the photoresponse in the short-wave spectral range. The $CrSiTe_3$–MoS_2 vdW heterodiode was fabricated using the tray transfer technique, in which $CrSiTe_3$ acts as MWIR light-absorbing material

X. Hu, J. Hou, Q. Dong, Z. Liu, S. Wang, Y. Tu, T. Han, F. Li, Z. Zhang, X. Hou, S. Wang, L. Shan, M. Long
Information Materials and Intelligent Sensing Laboratory of Anhui Province
Key Laboratory of Structure and Functional Regulation of Hybrid Materials of Ministry of Education
Institutes of Physical Science and Information Technology
Anhui University
111 Jiu Long Road, Hefei 230601, China
E-mail: lshan@ahu.edu.cn; longms@ahu.edu.cn

F. Wang
State Key Laboratory of Infrared Physics
Shanghai Institute of Technical Physics
Chinese Academy of Sciences
500 Yu Tian Road, Shanghai 200083, China
E-mail: fwang@mail.sitp.ac.cn

D. Zhao
State Key Laboratory of Luminescence and Applications
Changchun Institute of Optics
Fine Mechanics and Physics
Chinese Academy of Sciences
3888 Dongnanhu Road, Changchun 130021, China

The ORCID identification number(s) for the author(s) of this article can be found under https://doi.org/10.1002/aelm.202200208.

DOI: 10.1002/aelm.202200208

and *p*-type semiconductor. An ultrabroad band photodetection from 0.52 to 10.6 µm was demonstrated at room temperature based on the $CrSiTe_3$–MoS_2 vdW heterodiode. High specific detectivity D^* of 1.3×10^{11} cm $Hz^{1/2}$ W^{-1} was obtained in the visible range. The high-performance uncooled LWIR photodetection includes the R of 0.2 A W^{-1} and noise-equivalent power as low as 0.66 pW $Hz^{-1/2}$, and D^* of 1.93×10^9 cm $Hz^{1/2}$ W^{-1}, which were demonstrated at 10.6 µm laser under a bias of a –1 V.

2. Results and Discussion

$CrSiTe_3$ single crystal was grown using a self-flux method. The crystal structure of $CrSiTe_3$ is rhombohedral and it crystallized in the *R*-3 space group (space group No. 148), as shown in **Figure 1**a. Each unit cell comprises three $CrSiTe_3$ layers stacked in ABC order with alternating Te-Cr-Te and Te-Si-Te sandwich structures. The distance between the $CrSiTe_3$ layers is 3.3 Å.[20] The magnetism originates from the 3d orbital of Cr^{3+}, whose ferromagnetism is aligned along the *c*-axis, as indicated by the black arrows in Figure 1a. To characterize the structure of $CrSiTe_3$, single-crystal X-ray diffraction (XRD) measurements were performed. The XRD data in Figure 1b shows that there are only three distinct peaks corresponding to the (003), (006), and (0012) planes, indicating that high-quality $CrSiTe_3$ was obtained. The optical image of the $CrSiTe_3$ single crystal is presented in the inset of Figure 1b. The Raman spectrum of $CrSiTe_3$ in Figure 1c shows two obvious peaks at 118.8 and 138.6 cm^{-1} corresponding to E_g^3 and A_g^3 mode (out-of-plane vibrations of Te atoms).[21] The other three weak peaks located at 86.1, 214.2, and 358.6 cm^{-1}, corresponding to the E_g^1, E_g^4, and E_g^5 modes, respectively, which are well consistent with previous reports.[14,21,22] Elemental analysis of the crystals on cleaved surfaces was performed using energy-dispersive X-ray spectroscopy. As shown in Figure S1a (Supporting Information), the main peaks originated from Te, Si, and Cr elements. The atomic ratio Cr/Si/Te is 19.79:21.40:58.81, which is very close to 1:1:3 as shown in the inset of Figure S1a (Supporting Information).

The magnetization behavior of the $CrSiTe_3$ flake was characterized by the measurement of *M*–*H* and *M*–*T* curves. The magnetic field was applied parallel to the *ab* plane along the *c*-axis perpendicular to the easy axis of magnetization.[14] As shown in Figure 1d, the temperature-dependent magnetization curves during zero field-cooled (ZFC) and field-cooled (FC) were measured at H = 1 k Oe. As shown in the inset of Figure 1d, the critical temperature T_c = 33.4 K for the paramagnetic (PM) to ferromagnetic (FM) transition was extracted

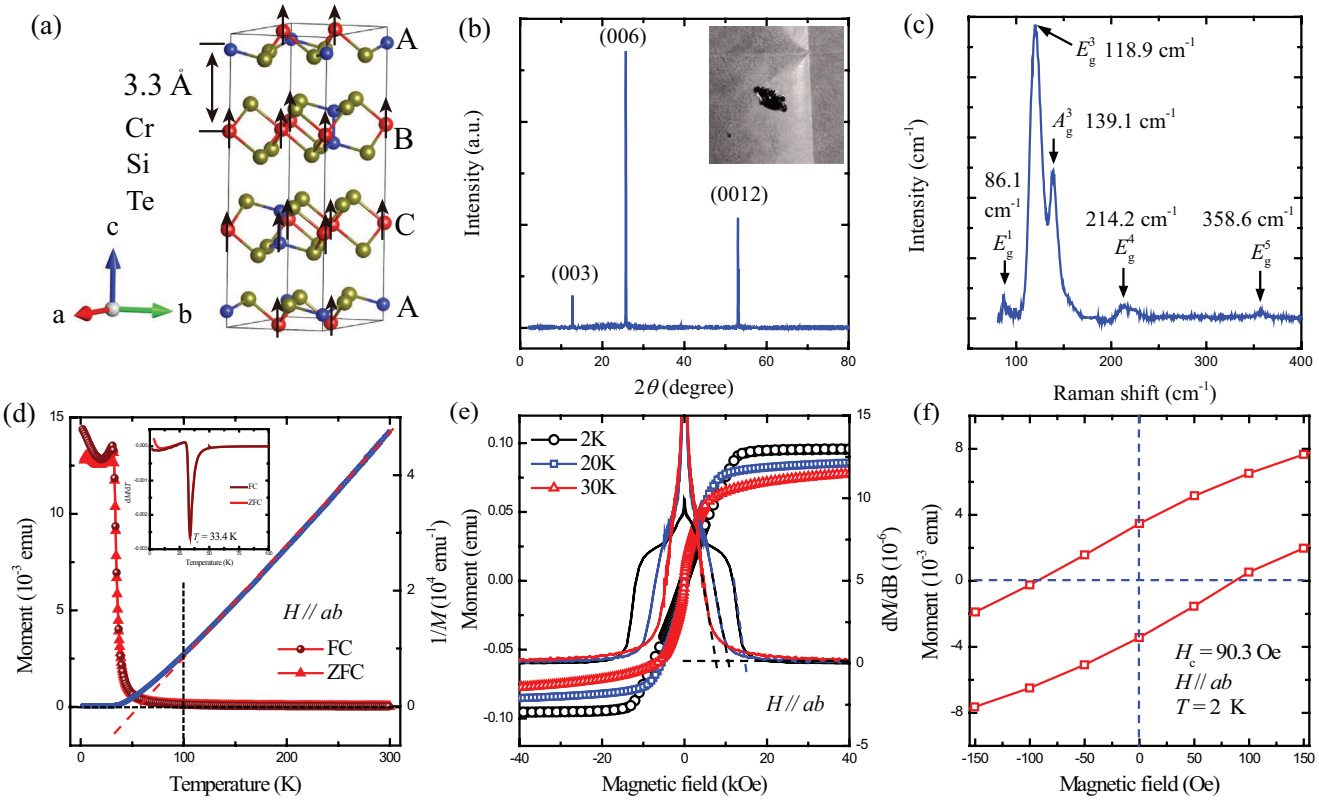

Figure 1. The magnetic properties characterization of $CrSiTe_3$ single-crystal. a) Schematic illustration of the $CrSiTe_3$ unit cell. The spin is indicated by the black arrows. b) Single-crystal X-ray diffraction (XRD) pattern of a $CrSiTe_3$ single crystal. The inset is an optical image of a single crystal with a shining *ab* planar surface. c) Raman spectrum of $CrSiTe_3$ thin film. d) Temperature dependence of magnetization measured at 1 k Oe magnetic field in zero field-cooled (ZFC) process and field-cooled (FC) process. The magnetic field is applied parallel to the *ab* plane. Inset: the derivative magnetization dM/dT as a function of temperature. The reciprocal of magnetization ($1/M$) as a function of the temperature is plotted on the right *y*-axis. e) Magnetic field dependence of magnetization (*M*–*H*) curves at 2, 20, and 30 K. f) Magnified *M*–*H* curve at 2 K.

from the minimum of the dM/dT curve, which is consistent well with the previous work.[14,20,23] The $1/M$ as a function of temperature is plotted on the right y-axis of Figure 1d. The red dashed line is the linear fit of $1/M$ versus temperature, which fits well in the range of 100–300K. Below 100 K, the $1/M$–T curve deviates from linear temperature-dependent behavior. The paramagnetic Curie temperature T_P = 55 (1) K is obtained, which is slightly lower than the previous work of 60 (2) K.[14] The magnetic hysteresis loops at various temperatures are shown in Figure 1e. When the magnetic field of H = 1 k Oe was applied in the ab plane at 2 K, the magnetization saturation of 14.8 k Oe is in good agreement with the previously literature.[14] An enlarged view of the hysteresis curve at 2 K is plotted in Figure 1f. The coercive field of $H//c$ at 2 K is 90.3 Oe, which is larger than that of 68 Oe at 5 K[20] and lower than that of 183 (2) Oe at 4.15 K.[24] The remanent magnetization is 0.004 emu.

To explore the optoelectrical properties of $CrSiTe_3$, we investigated the electron transport properties of $CrSiTe_3$ phototransistors. As shown in Figure S1b (Supporting Information), the transfer curve of typical $CrSiTe_3$ was measured at a back-gate voltage from −60 to 60 V at a bias of V_{ds} = 3 V. The inset of Figure S1b (Supporting Information) is an optical image of a typical $CrSiTe_3$ field-effect transistor. The typical p-type semiconductor transport behavior is observed. At V_g = −60 and 60 V, the source and drain current I_{ds} are 71.3 nA and 44.9 pA, respectively, with an on–off ratio >10^3. The room temperature mobility μ_B = 0.12 cm^2 V^{-1} s^{-1} was calculated using the formula $\mu = \frac{L}{WC_{ox}V_{ds}} \mathrm{d}I/\mathrm{d}V_g$. The $\mathrm{d}I_{ds}/\mathrm{d}V_g$ was extracted from the transfer curves I_{ds}–V_{bg}, where L is the channel length, W is the channel width, V_{ds} = 3 V and C_{ox} = 1.15 × 10^{-8} F cm^{-2} is the capacitance of 300 nm SiO_2 ($C_{ox} = \mu_0\mu_r/d_{ox}$, μ_0 = 8.85 × 10^{-12} F m^{-1}, and μ_r = 3.9). The hole mobility of our device is an order of magnitude larger than the previously reported 0.01 cm^2 V^{-1} s^{-1},[25] indicating that high-quality $CrSiTe_3$ samples were obtained. To examine the photoresponse of $CrSiTe_3$, we fabricated a p–n junction by dry transfer technique using such p-type $CrSiTe_3$ and n-type MoS_2. The Raman spectrum of MoS_2 is presented in Figure S1c (Supporting Information). The two vibration modes of in-plane $E_{2g}{}^1$ and out-of-plane A_{1g} are located at ≈381.9 cm^{-1} and 407.65 cm^{-1} respectively, which is consistent well with the previous report.[26] The thickness of a typical $CrSiTe_3$–MoS_2 was checked by atomic force microscopy (AFM). Figure S2a (Supporting Information) presents an optical image of a typical $CrSiTe_3$ phototransistor. The temporal photoresponse under various incident light power at a bias of 3 V is plotted in Figure S2b (Supporting Information). The extracted photoresponsivity (R) and external quantum efficiency (EQE) versus incident light power are shown in Figure S2c (Supporting Information). The R of 1.0 A W^{-1} and corresponding EQE of 202.9% was demonstrated. The time-resolved photoresponse in the MWIR and LWIR as a bias of −2 V is presented in Figure S2d (Supporting Information). The optical micrograph and AFM image of typical $CrSiTe_3$–MoS_2 are presented in Figure S3a,b (Supporting Information). The thickness of $CrSiTe_3$ is 38.7 nm and that of MoS_2 is 11.6 nm as shown in Figure S3c,d (Supporting Information), which are line scans along the white dashed lines in Figure S3b (Supporting Information). We first measured the I–V curve as shown in **Figure 2**a. The typical p–n junction transport behavior is observed with a rectification ratio >10.[2] The ideality factor n was used to evaluate the rectifying performance, which was estimated by fitting to the Shockley diode equation $I_d = I_s\left[\exp\left(\frac{V_d}{nV_T}\right)-1\right]$[27] where I_s is reverse saturation current, the $V_T = k_BT/q$ represents the thermal voltage. Notably, the ideality factor n ≈1.3 was extracted from the forward bias at the idea linear diode region, as shown in the inset of Figure 2a. Compared with the conventional silicon p–n diode ($1 \le n \le 2$),[28] the low ideality factor n indicates a low charge trap density at the interface of the junction. When the thickness of $CrSiTe_3$ and MoS_2 is in the range of 30–50 nm, and 5–15 nm, respectively, the p–n junction devices with high light absorption and good rectification can be realized. To character the electric transport behavior of the $CrSiTe_3$–MoS_2 heterodiode, we next investigated the photoresponse of this $CrSiTe_3$–MoS_2 p–n junction. The I–V curves were measured under a 637 nm laser with various incident light power, as presented in Figure 2b. The open-circuit voltage V_{OC} and short circuit current I_{SC} increase with the increase of optical power. The extracted V_{oc} and I_{sc} as functions of power are presented in the inset of Figure 2b. The V_{oc} = 0.135 V and I_{SC} = 233.52 nA are realized under incidence light power of 9.51 μW. To explore the photovoltaic response, the temporal photoresponse of a typical $CrSiTe_3$–MoS_2 p–n junction at various incident light powers is plotted in Figure S4a (Supporting Information). The light power-dependent photocurrent is presented in Figure S4b (Supporting Information). A power-law relationship $I_P \propto P^\alpha$ with α = 0.95 <1, a sublinear power dependence was observed. To further confirm the photovoltaic response originates from the $CrSiTe_3$–MoS_2 p–n junction rather than the Schottky barrier during metal contact, we measured spatially resolved photocurrent mapping at zero bias, as shown in Figure S4c (Supporting Information), the scale bar is 5 μm. Compared with the optical micrograph as shown in Figure S4d (Supporting Information), it is obvious that the photocurrent mainly originates from the region of the $CrSiTe_3$–MoS_2 junction. It further confirms that a built-in electric field was formed in the junction area. To quantitatively evaluate the performance of this p–n junction, we calculated the R and EQE at V_{ds} = 0 V and V_{ds} = −1.5 V via the following formulas, $R = I_P/P_L$, and $EQE = hcR/e\lambda$, where I_P is the photocurrent, P_L is the incident light power, h is the Planck's constant and c is the speed of light and λ is the wavelength of incident light. The photovoltaic response R and EQE as a function of light power are presented in Figure 2c. The photovoltaic response R shows weak light power dependence. The light power varies from 439.5 to 45.7 μW, the R fluctuation from 0.15 to 0.12 A W^{-1}, corresponding to EQE fluctuation from 29.7% to 23.5%. The highest photovoltaic response of 0.15 A W^{-1} is realized, which is larger than that of 0.12 A W^{-1} of the multi-layer MoS_2–WSe_2 p–n junction,[29] indicating that this $CrSiTe_3$–MoS_2 p–n junction can be used as a good photovoltaic detector. The p–n junction has good rectification performance, and the detector can operate at extremely low dark current under reverse bias. The light power dependence R and EQE at a reverse bias of −1.5 V are presented in Figure 2d. At low incident power densities, a saturation trend of R appears. As the light power increases, R and EQE decrease. Photoconductive gain is defined as the ratio of the number

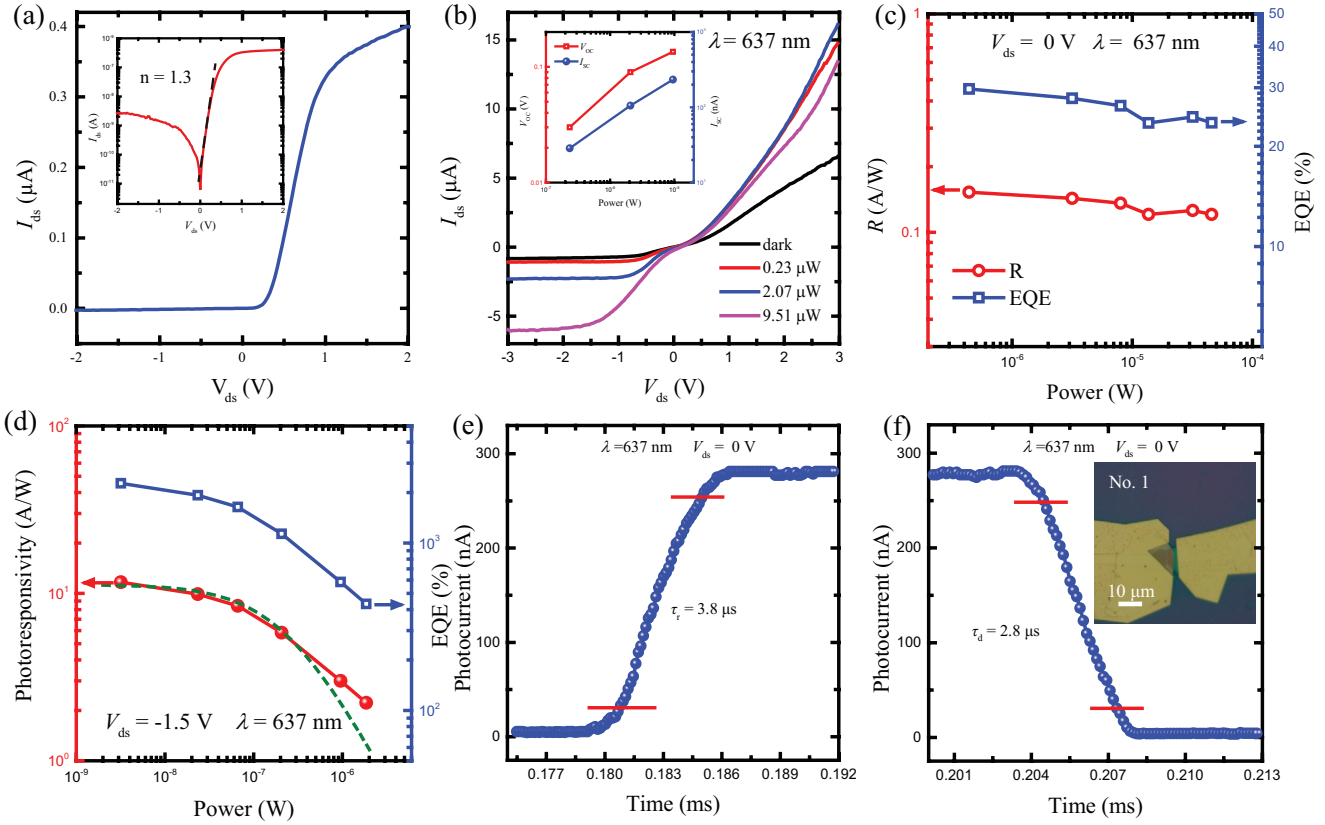

Figure 2. Optoelectrical properties characterization of typical $CrSiTe_3$–MoS_2 heterostructure device. a) The *I–V* curve of the $CrSiTe_3$–MoS_2 heterostructure devices. Inset: Semi-logarithmic plot of the *I–V* curve. The blue dash line is linearly fitted to the diode equation and obtains an ideality factor of $n \approx 1.3$. b) The output characteristic curves of the device under the dark condition and a 637 nm laser with varying light powers. c) Photovoltaic *R* and EQE as a function of incident light power. d) Incident light power-dependent of the *R* (red solid circle) and EQE (blue open square) of a typical $CrSiTe_3$–MoS_2 photodetector at reverse bias $V_{ds} = -1.5$ V in ambient. e,f) Time-resolved photoresponse of the device at $V_{ds} = 0$ V. The photoresponse has a rise time of 3.8 μs and a decay time of 2.8 μs. Inset: the optical image of the device.

of electrons collected per unit time to the number of photons absorbed per unit time ($G = N_e/N_P$),[30]

$$G = \frac{N_e}{N_P} = \frac{I_P}{eF} = \frac{\tau_0}{\tau_t} \frac{1}{1+(F/F_0)^m} \quad (1)$$

where F is the photon absorption rate, τ_0 is the carrier lifetime at low excitation density, F_0 is the photon absorption rate when trap saturation occurs, and n is the phenomenological fitting parameter. The transit time $\tau_t = L^2 \mu^{-1} V_{ds}^{-1}$, where μ is the carrier mobility and L is the channel length.

The speed of photoresponse is one of the key figure-of-merit of photodetectors. To check the performance of this $CrSiTe_3$–MoS_2 p–n junction, we measured the photoresponse time using a 637 nm laser with a pause frequency of 1 Hz. The rise τ_r and decay time τ_d are defined as the steady photocurrent rising from 10% to 90% and decaying from 90% to 10% after turning on/off the light, respectively. The $\tau_r = 3.8$ μs and $\tau_d = 2.8$ μs were obtained, as shown in Figure 2e,f. The response time is much faster than most other 2D materials detectors summarized in Table S1 (Supporting Information) for comparison. The temporal photoresponse in the visible range at 520 nm at a 1 V bias and the photovoltaic response in the near-infrared 830 nm under a –2 V bias is plotted in Figure S5a,b (Supporting Information), respectively.

To study the photoresponse in the short-wave infrared range, we systematically measured the photoresponse at various incident light power densities. As shown in **Figure 3**a, the current of the 1310 nm laser at different light powers is much higher than that of the device operating in dark. In the *I–V* curves with and without light, the photocurrent at reverse bias is much higher than that of the forward bias. The optical image of the measuring device is shown in the inset of Figure 3a. The light power dependence of the *R* and EQE at a –1 V bias is presented in Figure 3b. The *R* of up to ≈20.7 A W^{-1} and EQE of 4031.71% can be realized at the 1310 nm laser. The EQE is well above 100%, indicating the presence of photo gain in this p–n junction device. The time-resolved photoresponse of a typical $CrSiTe_3$–MoS_2 heterostructure placed on the prefabricated electrodes at 1 V bias under various incident light powers is presented in Figure 3c. The photocurrent up to 26.3 μA is demonstrated under the light power of 1.6 μW. The light power-dependent photocurrent was then extracted, as shown in Figure 3d. A sublinear light power-dependent behavior is observed with $\alpha = 0.99 < 1$. The photocurrents under various light powers were extracted from the *I–V* curves in Figure 3c. The optical image of the device is shown in the inset of Figure 3d.

The narrow bandgap $CrSiTe_3$ is a prospective candidate for mid-wave infrared photodetection. Aiming for this goal, we

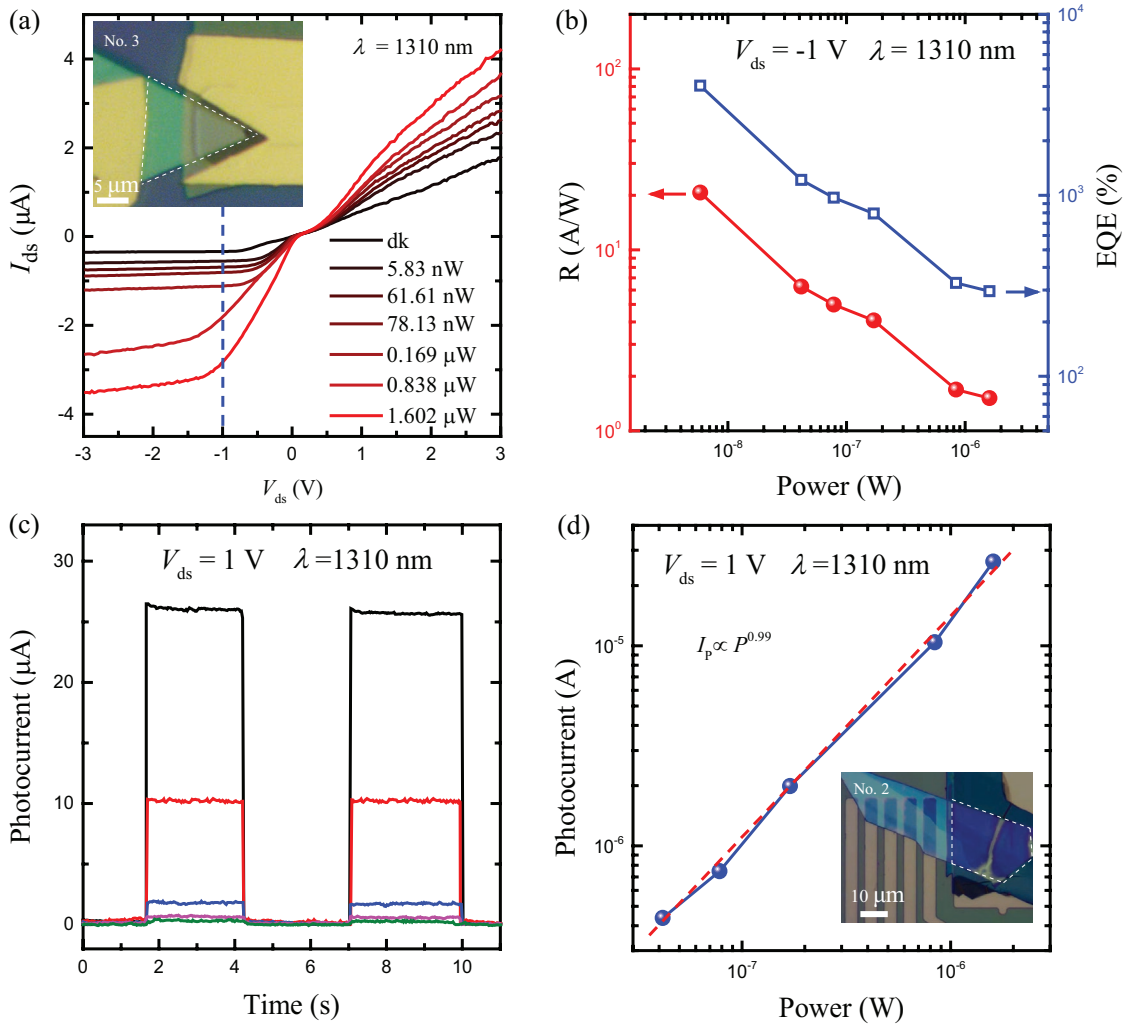

Figure 3. Photoresponse of a typical $CrSiTe_3$–MoS_2 heterostructure at short-wave infrared. a) *I–V* curves of a typical $CrSiTe_3$–MoS_2 heterostructure under a 1310 nm laser with various incident powers and without light incident. Inset: the optical image of the measuring device. b) The extracted photoresponsivity *R* and EQE as a function of 1310 nm laser power at –1 V bias. c) Temporal photoresponse of $CrSiTe_3$–MoS_2 heterostructure under 1 V bias at different light powers of 1310 nm. d) The light power-dependent photocurrent under 1310 nm laser at 1 V bias. Inset: the optical image of the device measured in Figure 3c.

measured the photoresponse of this $CrSiTe_3$–MoS_2 using a continuous-wavelength mid-wave infrared laser as the excitation light. The *I–V* curves were measured under a laser of 3403 nm with various incident powers and dark, as shown in **Figure 4**a. In the reverse bias range, the current saturates rapidly. The onset saturation voltage (V_{sat}) is related to the incident light power. At V_{ds} = –1 V, marked by the blue dash line to guide the eyes in Figure 4a, the current saturates at low incident light powers from 0.46 to 5.94 μW. Under higher light powers (from 7.43 to 13.37 μW), the current does not saturate and increases linearly with increasing bias. Then, we extracted the photocurrent at V_{ds} = –2 V and calculated *R* and EQE, as shown in Figure 4b. In the low power range from 0.46 to 3.39 μW, *R*, and EQE decreased from 0.47 to 0.11 A W^{-1} and 17.3% to 3.9%, respectively, with increasing light power. At relatively higher power intensities, from 3.39 to 11.04 μW, the *R* and EQE exhibit small fluctuations from 0.10 to 0.12 A W^{-1} and from 3.6% to 4.3%, respectively. In the MWIR range, we also systematically measured the photoresponse at 2611 and 3662 nm. The temporal photoresponse at a 1 V bias was presented in Figure S6a (Supporting Information). The photocurrent up to 268.7 nA was obtained at a 1 V bias under 0.31 μW illumination power. The *I–V* curves with varying the light power and without light incident are plotted in Figure S6b (Supporting Information). Then the photocurrents were extracted at a –1 V bias and plotted as a function of power in Figure S6c (Supporting Information). A super-linear power dependence is observed with a power exponent $\alpha = 1.19$. The incident light power-dependent of the *R* and EQE under the 2611 nm laser were calculated and presented in Figure S6d (Supporting Information). As the light power increases from 11.2 to 492.8 nW at a bias of –1 V, *R* slightly increases from 0.51 to 1.15 A W^{-1}, and the corresponding EQE increases from 23.9% to 54.9%. The *I–V* curves were measured by varying the power of the 3662 nm laser from 0.08 to 1.49 μW under dark, as shown in Figure S7a (Supporting Information). The extracted photocurrent at a –1 V bias as a function of light power, as

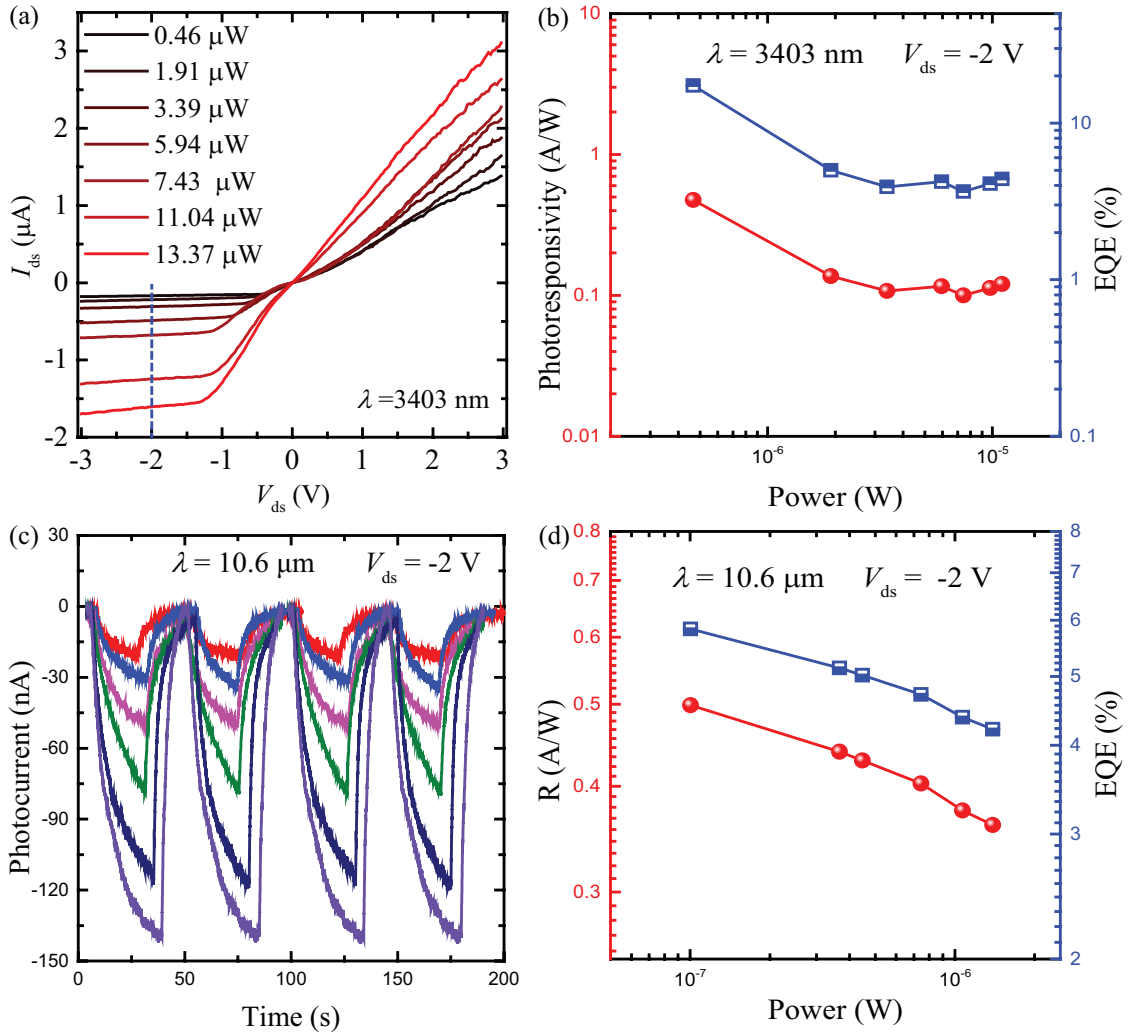

Figure 4. The photoresponse of a typical $CrSiTe_3$–MoS_2 heterostructure device at MWIR and LWIR. a) The *I*–*V* curves of $CrSiTe_3$–MoS_2 heterostructure excited by MWIR 3403 nm light with various power from 0.46 to 13.37 μW. b) The light power-dependent photocurrent of MWIR 3403 nm light at −1 V bias. c) Time-resolved photoresponse of the $CrSiTe_3$–MoS_2 heterostructure detector under various light powers of 10.6 μm laser at V_{ds} = −2 V. The measurements were carried out at −2 V under a 10.6 μm laser in ambient. d) *R* and EQE as a function of incident light power of 10.6 μm laser at −2 V.

shown in Figure S7b (Supporting Information). A superlinear light power-dependent behavior is observed at power exponent $\alpha = 1.05$. Then the *R* and EQE under 3662 nm laser at a −1 V bias were calculated and presented in Figure S7c (Supporting Information). The *R* fluctuated from 0.26 to 0.44 A W^{-1} and EQE fluctuated from 8.8% to 14.9% as the power ranged from 23.9 nW to 1.49 μW. The dependence of the photocurrent on the light power incident to the device follows a power-law relationship $I_P \propto P^{\alpha}$, where $\alpha = 1$, and the photocurrent increases linearly with the light power, indicating that the number of photogenerated carriers is proportional to the number of incidence photons. The nonlinear light power dependence is the result of complex processes in the photoresponse, including electron–hole generation, trapping, and photocarriers recombination.[31] The sublinear light power-dependent behavior ($\alpha < 1$) implies a new route for photoexcited carriers through recombination loss, which has been reported in other materials, such as in MoS_2,[32–34] InSe,[35] ZnO nanowires,[36] GaN nanowires,[37] and Germanium nanowires.[38] However, the superlinear dependence behavior ($\alpha > 1$) was observed in monolayer $MoS_{2(1-x)}Se_{2x}$[39] and Ta_2NiSe_5[40] ($\alpha = 1.1$), which are relatively rare compared with sublinear and linear light power dependence. The theoretical model for understanding the superlinear behavior requires the presence of recombination centers and capture cross-sections. As the light power increases, the recombination centers are passivated gradually, resulting in an increased lifetime of the photoexcited carriers. The superlinear behavior has also been observed in single crystal As_2S_3 with $\alpha = 1.7$,[41] Mg/$ZnSnP_2$/Sn Schottky junction ($\alpha = 1.42 \pm 0.21$, 1.75 ± 0.19),[42] $Cs_2Hg_6S_7$ single crystals $\alpha = 1.45$,[43] and graphene quantum dot-like arrays structure ($\alpha = 1.07$).[31] The temporal photoresponse at a 1 V bias under 3662, 3089, and 3908 nm laser are presented in Figure S7d–f (Supporting Information). The incident light power was 0.84 μW and a photocurrent of 230 nA were obtained under a 3662 nm laser. The photocurrent is as high as 681.1 nA under the 3089 nm laser with an incident light power of 1.32 μW and

127.7 nA under the 3809 nm laser with a light power of 0.51 μW were demonstrated, indicating that a good MWIR response was achieved.

Next, we characterized the long-wave infrared photoresponse. The *I*–*V* curves under various light power and dark are plotted in Figure S7g (Supporting Information). The time-resolved photoresponse under various powers of 10.6 μm laser at a −2 V bias is presented in Figure 4c. Then, the incident light power-dependent photocurrent extracted from the temporal photoresponse is plotted in Figure S7h (Supporting Information). A sublinear power dependence was observed at $\alpha = 0.97$, which is very close to the linear dependence. The *R* and EQE were calculated and presented in Figure 4d. As the power increases from 0.10 to 1.38 μW, the photoresponsivity shows that the slit decrease from 0.50 to 0.36 A W^{-1}, and the corresponding EQE decreases from 5.8% to 4.2%. The temporal photoresponse of this typical p–n junction device was measured under a 10.6 μm laser in ambient, as shown in Figure S7i (Supporting Information). A photocurrent as high as ≈120 nA was obtained, indicating that the device has excellent room temperature long-wave infrared detection capability.

Notably, the ultra-broadband photoresponse from 0.52 to 10.6 μm based on $CrSiTe_3$–MoS_2 heterostructure was demonstrated. The photoresponsivity and EQE at a −1 V bias as a function of wavelength are presented in **Figure 5**a. In the visible and short-wave infrared range, the photoresponsivity is up to 14.3 A W^{-1} and the EQE up to 2791%, indicating high photo gain is operated in this range. In the mid-wave infrared range, a photoresponsivity range from 0.22 to 0.63 A W^{-1} and EQE range from 6.5% to 30.2% was realized. In the long-wave range of 10.6 μm, the photoresponsivity is 0.20 A W^{-1} and the EQE is 2.36%.

To check the sensitivity of these $CrSiTe_3$–MoS_2 heterostructure devices, we measured the current noise power density spectrum at a −1 V bias, as shown in Figure 5b. The current

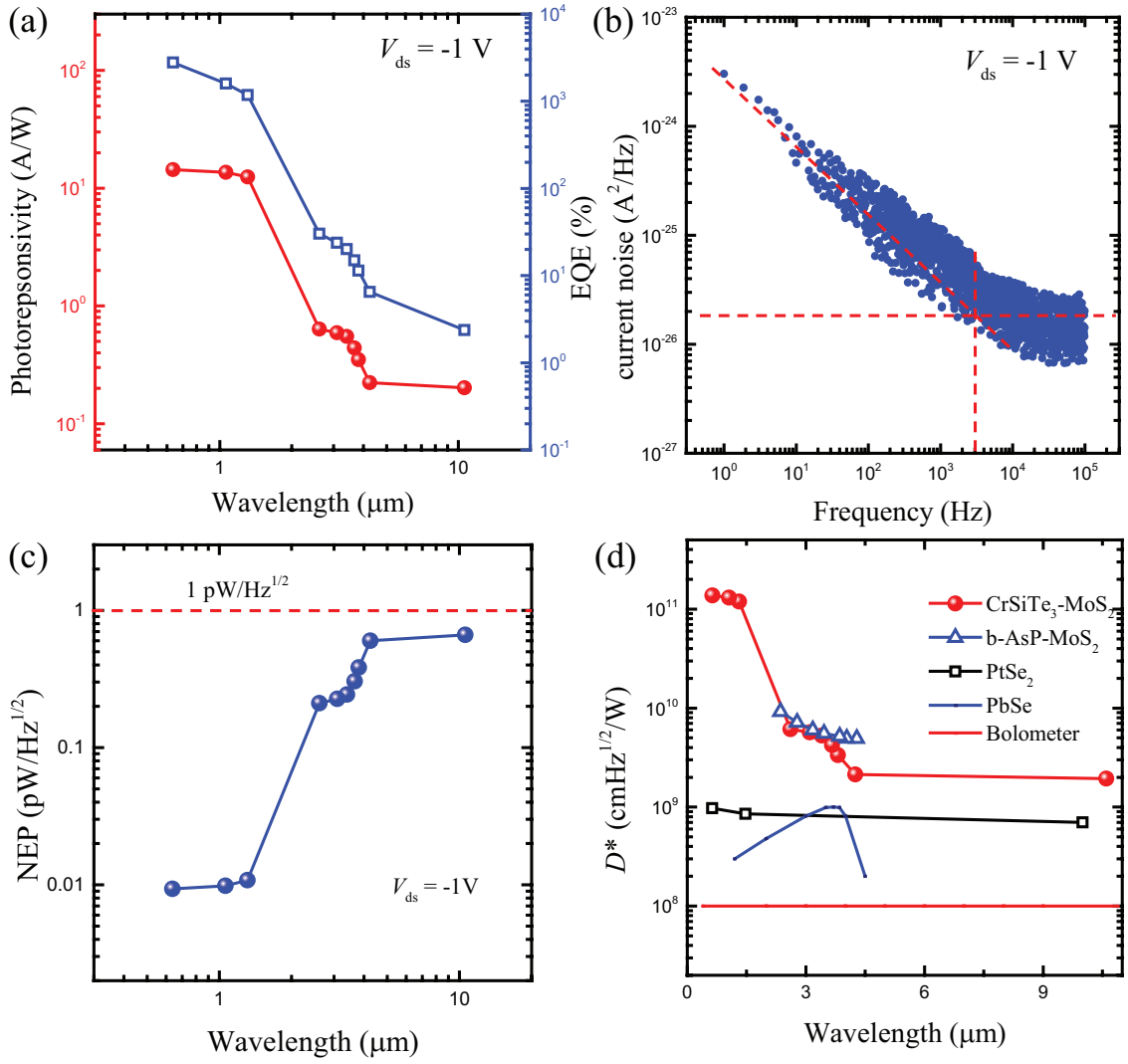

Figure 5. The performance of $CrSiTe_3$–MoS_2 heterostructure photodetectors. a) Extracted wavelength-dependent photoresponsivity *R* (red solid circles) and EQE (blue open circles) of the $CrSiTe_3$–MoS_2 photodetector at V_{ds} = −1 V in ambient. b) Noise current power spectrum of $CrSiTe_3$–MoS_2 heterojunction photodetector at −1 V bias. c) Wavelength-dependent noise equivalent power of incident light for $CrSiTe_3$–MoS_2 photodetector at V_{ds} = −1 V in ambient. d) The specific detectivity D^* of various 2D materials and conventional infrared materials as a function of wavelength at room temperature.

noise power density spectra at various biases are presented in Figure S8 (Supporting Information). In the low-frequency range, 1/f noise dominates the noise power contribution. When the frequency is larger than 3 kHz, the noise current power density spectrum becomes frequency-independent, showing white noise behavior. All Johnson noise, shot noise, and generate-recombination noise (G–R noise) is white noise. For the cm $Hz^{1/2}$ W^{-1} noise, it can be expressed as $\langle i_n^2 \rangle = 4k_B T\Delta f/R_0$, where k_B is the Boltzmann constant, T is the temperature, Δf is the bandwidth, and R_0 is the resistance of the device in dark. Then we calculated the Johnson noise $\langle i_n^2 \rangle = 8.6 \times 10^{-29}$ A^2, where R_0 = 192.3 MΩ was measured at a –1 V bias in dark, T = 300 K and Δf = 1 Hz, which is three orders of magnitude lower than the experimental results. The short noise could be calculated as $\langle i_n^2 \rangle = 2eI_{dark}\Delta f = 1.66 \times 10^{-27}$ A^2 with I_{dark} = 5.2 nA and Δf = 1 Hz. The G–R noise is often observed in low-frequency $f < 1/(2\pi\tau)$, the noise current can express as $\langle i_n^2 \rangle = S_0/[1+(2\pi\tau)^2]$,[44] where S_0 is the frequency-independent portion, τ is the time constant associated with a specific trapping state. The shot noise is the major contribution of noise current in the high-frequency range. Then we calculate one of the most important figures of merits, the noise equivalent power (NEP), defined as the measured noise current over the photoresponsivity (NEP = i_n/R), commonly used to evaluate the sensitivity of photodetectors. As shown in Figure 5c, the NEP is lower than 0.66 pW $Hz^{-1/2}$ in the long-wave infrared range, 0.21–0.60 pW $Hz^{-1/2}$ in the mid-wave infrared range, and below 0.01 pW $Hz^{-1/2}$ in the visible and near-infrared range, indicating that this $CrSiTe_3$–MoS_2 heterostructure detector can distinguish the minimum of 0.66 pW long-wave infrared and 0.01 pW short-wave light signal from noise. Then we calculate the specific detectivity D^*, which is used for evaluating the performance of the detector to eliminate the effective area of the device (A) and the electrical bandwidth (Δf). The value of the specific detectivity could be calculated by $D^* = (A\ \Delta f)^{1/2}/\mathrm{NEP}$. The D^* of the $CrSiTe_3$–MoS_2 heterostructure detector from visible to long-wave infrared is presented in Figure 5d. At the long-wave infrared 10.6 μm, a D^* as high as 1.93×10^9 cm $Hz^{1/2}$ W^{-1} was obtained, which is higher than the previously reported $PtSe_2$ ($\approx 7 \times 10^8$ cm $Hz^{1/2}$ W^{-1}) and one order of magnitude higher than of commercial bolometer. In the mid-wave infrared range of 2.6–4.3 μm, the D^* ranges from 2.1×10^9 to 6.1×10^9 cm $Hz^{1/2}$ W^{-1}, which is much higher than commercial PbSe detectors. Compared with the $PdSe_2$–MoS_2 photodetector in the previous report,[45] this D^* is as high as 1.4×10^{11} cm $Hz^{1/2}$ W^{-1} in the visible and short infrared range, which is one order of magnitude higher than that of $PdSe_2$–MoS_2 photodetector. In the mid-wave infrared range of 2.6–4.3 μm, the D^* is comparable to b-PAs-MoS_2[46] and slightly lower than the $PdSe_2$–MoS_2 photodetector. It is worth mentioning, that this $CrSiTe_3$–MoS_2 heterostructure detector is stable in ambient. The photocurrent did not decay after the device was exposed to the air for more than one year, as shown in Figure S9a–f (Supporting Information). The performance of broadband heterostructure photodetectors is summarized in Table S1 (Supporting Information) for comparison. The speed of photoresponse in MWIR is shown in Figure S10 (Supporting Information). The rise time of 9 s and the decay time of 6 s was demonstrated.

3. Conclusion

In summary, we synthesized a high-quality ferromagnetic 2D semiconductor $CrSiTe_3$. We systematically studied the ferromagnetic behaviors of $CrSiTe_3$ single crystal and opto-electrical properties of $CrSiTe_3$–MoS_2 heterostructures. High photoresponsivity up to 20.7 A W^{-1} and EQE up to 4031.7% were achieved at 1310 nm. Ultrabroadband from 0.52 to 10.6 μm and specific detectivity > 1.93×10^9 cm $Hz^{1/2}$ W^{-1} were realized at room temperature. Further work may investigate the ferromagnetic transition and spin injection in $CrSiTe_3$–MoS_2 heterostructures and valley-polarized devices for infrared polarized light detection. The results show that the $CrSiTe_3$ is promising for uncooled long-wave infrared detection, which is of great significance for the high-generation and detection of highly sensitive polarized light.

4. Experimental Section

Materials Synthesis: $CrSiTe_3$ single crystals were synthesized using a self-flux method from high purity elemental Cr (99.99%), Si (99.99%), and Te (99.99%) material. A mixture of materials (an optimized ratio of Cr: Si: Te is 1: 2: 6 for $CrSiTe_3$) was sealed in evacuated quartz ampoules and heated at 1100 °C for 1 day. Then cooled to 800 °C at a rate of 1.5 °C h^{-1}, and then switched off the furnace and cooled to room temperature naturally. A platelet-sharp single crystal with metal luster and a size of several millimeters was obtained. The magnetism of the $CrSiTe_3$ single crystal in bulk was confirmed by a Magnetic Properties Measurement System (MPMS, Quantum Design).

Device Fabrication and Measurements: The $CrSiTe_3$–MoS_2 heterostructures were fabricated using the dry transfer technique. The multi-layer $CrSiTe_3$ and MoS_2 flakes were exfoliated on PDMS. Two methods were used to fabricate the $CrSiTe_3$–MoS_2 devices. The first one was that the heterostructure was transferred to the prepared electrodes which were fabricated on a silicon substrate covered by 300 nm SiO_2 by standard electron-beam lithography (EBL) process followed by standard electron-beam evaporation of the metal. Typically, the prepared electrode was 5-nm Ti and 30-nm Au in thickness. Before the transfer process, the electrodes were treated with oxygen plasma to realize good contact. The electrode treatment process was carried out using a homemade plasma cleaner. The power was set to ≈5 W and the treating process was carried out for 60 s. Another one was the $CrSiTe_3$–MoS_2 heterostructures were transferred on a Si/SiO_2 substrate. The electrodes were fabricated by the standard EBL and electron-beam evaporation Ti/Au (5/50 nm).

Electrical and photoresponse measurements were carried out using a dual-channel digital source meter (Keithley 2636B) in the ambient. Noise current density spectrum at –1 V bias was measured in a metal shielded box. Data were acquired using a noise measurement system (PDA NC300L, 100 kHz bandwidth).

The NEP and D^* at a bias of –1 V were calculated using the NEP = i_n/R. The current noise density spectrum was measured from 1 to 100 kHz electronic bandwidth at a bias of –1 V. The root-mean-square noise current $\langle i_n^2 \rangle^{1/2} = 1.34 \times 10^{-13}$ A $Hz^{-1/2}$ was calculated from $\langle i_n^2 \rangle = \frac{1}{B}\int_0^B S_n(f)df = 1.82 \times 10^{-26}$ A^2 Hz^{-1}. The D^* was calculated using $D^* = \sqrt{A\Delta f}/NEP$, where Δf is the electronic bandwidth of 1 Hz, A = 164.6 μm^2 is the area of the device, the detail is presented in the Supporting Information. The response time in Figure 2e was obtained from device 1, inset of Figure 2f. The photocurrent under SWIR 1310 nm in Figures 3c,d is extracted from device 2, inset of Figure 3d. The other for calculated NEP and D* were realized from device 3, as shown in the inset of Figure 3a.

Supporting Information

Supporting Information is available from the Wiley Online Library or from the author.

Acknowledgements

This work was supported by the National Natural Science Foundation of China (Grant Nos. 61975224 and 12074002), University Synergy Innovation Program of Anhui Province (Grant No. GXXT-2020-050), Fund of Anhui Provincial Natural Science Foundation (Grant No. 2008085MF206), National Key R&D Program of China (Grant No. 2017YFA0302904, 2018YFA0305602), Major Basic Program of Natural Science Foundation of Shandong Province (Grant No. ZR2021ZD01), Recruitment Program for Leading Talent Team of Anhui Province, 2019-16, and 2020, State Key Laboratory of Luminescence and Applications (Grant No. SKLA-2021-03), and Open Fund of Infrared and Low-Temperature Plasma Key Laboratory of Anhui Province (Grant No. IRKL2022KF03). The authors thank Professor Xiaomu Wang at Nanjing University for their experimental support and helpful discussion.

Conflict of Interest

The authors declare no conflict of interest.

Author Contributions

X.H. and J.H. contributed equally to this work. M.L., W.H., and L.S. conceived the project and designed the experiments. M.L., X.H., and Q.D. performed device fabrication and characterization. M.L., X.H., J.H., and W.H. performed data analysis and interpretation. M.L., X.H., J.H., and W.H. co-wrote the paper, and all authors contributed to the discussion and preparation of the manuscript.

Data Availability Statement

The data that support the findings of this study are available from the corresponding author upon reasonable request.

Keywords

2D materials, ferromagnetism, long-wave infrared photodetectors, photodetectors, van der Waals heterodiodes

Received: March 3, 2022
Revised: May 19, 2022
Published online: June 20, 2022

[1] B. Huang, G. Clark, E. Navarro-Moratalla, D. R. Klein, R. Cheng, K. L. Seyler, D. Zhong, E. Schmidgall, M. A. Mcguire, D. H. Cobden, W. Yao, Di. Xiao, P. Jarillo-Herrero, X. Xu, *Nature* **2017**, *546*, 270.
[2] C. Gong, L. Li, Z. Li, H. Ji, A. Stern, Y. Xia, T. Cao, W. Bao, C. Wang, Y. Wang, Z. Q. Qiu, R. J. Cava, S. G. Louie, X. J. Xia, *Nature* **2017**, *546*, 265.
[3] Z. Fei, B. Huang, P. Malinowski, W. Wang, T. Song, J. Sanchez, W. Yao, Di. Xiao, X. Zhu, A. F. May, W. Wu, D. H. Cobden, J.-H. Chu, X. Xu, *Nat. Mater.* **2018**, *17*, 778.
[4] Y. Deng, Y. Yu, Y. Song, J. Z. Wang, Z. Sun, Y. Yi, Z. Wu, S. Wu, J. Zhu, J. Wang, X. H. Chen, Y. Zhang, *Nature* **2018**, *563*, 94.
[5] B. Huang, G. Clark, D. R. Klein, D. Macneill, E. Navarro-Moratalla, K. L. Seyler, N. Wilson, M. A. Mcguire, D. H. Cobden, Di. Xiao, W. Yao, P. Jarillo-Herrero, X. Xu, *Nat. Nanotech.* **2018**, *13*, 544.
[6] S. Jiang, J. Shan, K. F. Mak, *Nat. Mater.* **2018**, *17*, 406.
[7] X. Wang, J. Tang, X. Xia, C. He, J. Zhang, Y. Liu, C. Wan, C. Fang, C. Guo, W. Yang, Y. Guang, X. Zhang, H. Xu, J. Wei, M. Liao, X. Lu, J. Feng, X. Li, Y. Peng, H. Wei, R. Yang, D. Shi, X. Zhang, Z. Han, Z. Zhang, G. Zhang, G. Yu, X. Han, *Sci. Adv.* **2019**, *5*, w8904.
[8] S. Jiang, L. Li, Z. Wang, K. F. Mak, J. Shan, *Nat. Nanotech.* **2018**, *13*, 549.
[9] Z. Wang, T. Zhang, M. Ding, B. Dong, Y. Li, M. Chen, X. Li, J. Huang, H. Wang, X. Zhao, Y. Li, D.a Li, C. Jia, L. Sun, H. Guo, Y.u Ye, D. Sun, Y. Chen, T. Yang, J. Zhang, S. Ono, Z. Han, Z. Zhang, *Nat. Nanotech.* **2018**, *13*, 554.
[10] I. A. Verzhbitskiy, H. Kurebayashi, H. Cheng, J. Zhou, S. Khan, Y. P. Feng, G. Eda, *Nat. Electron.* **2020**, *3*, 460.
[11] T. Li, S. Jiang, N. Sivadas, Z. Wang, Y. Xu, D. Weber, J. E. Goldberger, K. Watanabe, T. Taniguchi, C. J. Fennie, K. Fai Mak, *J. Nat. Mater.* **2019**, *18*, 1303.
[12] X. Wang, Z. Li, M. Hou, J. Zhao, L. Li, A. Rahman, Z. Xu, J. Gong, Z. Chi, R. Dai, Z. Wang, Z. Qiao, Z. Zhang, *Phys. Rev. B.* **2019**, *100*, 14407 .
[13] Y. Wang, C. Wang, S.-J. Liang, Z. Ma, K. Xu, X. Liu, L. Zhang, A. S. Admasu, S.-W. Cheong, L. Wang, M. Chen, Z. Liu, B. Cheng, W. Ji, F. Miao, *Adv. Mater.* **2020**, *32*, 2004533.
[14] L. D. Casto, A. J. Clune, M. O. Yokosuk, J. L. Musfeldt, T. J. Williams, H. L. Zhuang, M.-W. Lin, K. Xiao, R. G. Hennig, B. C. Sales, J.-Q. Yan, D. Mandrus, *APL Mater.* **2015**, *3*, 041515.
[15] M. Lin, et al., *J. Mater. Chem. C.* **2016**, *4*, 315.
[16] H. Ji, R. A. Stokes, L. D. Alegria, E. C. Blomberg, M. A. Tanatar, A. Reijnders, L. M. Schoop, T. Liang, R. Prozorov, K. S. Burch, N. P. Ong, J. R. Petta, *J. Appl. Phys.* **2013**, *114*, 114907.
[17] H. L. Zhuang, Y.u Xie, P. R. C. Kent, *Phys. Rev. B.* **2015**, *92*, 35407.
[18] M. Razeghi, B. M. Nguyen, *Rep. Prog. Phys.* **2014**, *77*, 082401.
[19] J. Liu, F. Xia, D. Xiao, G. De Abajo, *Nat. Mater.* **2020**, *19*, 830.
[20] S. Wu, L. Wang, B. Gao, Y. Wang, Y. S. Oh, S.-W. Cheong, J. Hong, X. Wang, *AIP Adv.* **2018**, *8*, 055016.
[21] A. Milosavljević, A. Šolajić, J. Pešić, Y. Liu, *Phys. Rev. B.* **2018**, *98*, 104306.
[22] Q. Xie, Y. Liu, M. Wu, H. Lu, W. Wang, L. He, Y. Liu, *Mater. Lett.* **2019**, *246*, 60.
[23] V. Carteaux, F. Moussa, M. Spiesser, *Euro. Phys. Lett.* **1995**, *29*, 251.
[24] V. Carteaux, G. Ouvrard, J. C. Grenier, Y. Laligant, *J. Mag. Mag. Mater.* **1911**, *94*, 127.
[25] M.-W. Lin, H. L. Zhuang, J. Yan, T. Z. Ward, A. A. Puretzky, C. M. Rouleau, Z. Gai, L. Liang, V. Meunier, B. G. Sumpter, P. Ganesh, P. R. C. Kent, D. B. Geohegan, D. G. Mandrus, K. Xiao, *J. Mater. Chem. C.* **2016**, *4*, 315.
[26] C. Lee, H. Yan, L. E. Brus, T. F. Heinz, J. Hone, S. Ryu, *ACS Nano* **2010**,*4*, 2695.
[27] T. C. B. A. Jayakumar, *Elec. Lett.* **2000**, *36*, 291.
[28] M. El-Tahchi, A. Khoury, M. De Labardonnie, P. Mialhe, F. Pelanchon, *Sol. Ener. Mater. & Sol. Cell.* **2000**, *62*, 393.
[29] C.-H.o Lee, G.-H. Lee, A. M. Van Der Zande, W. Chen, Y. Li, M. Han, X. Cui, G. Arefe, C. Nuckolls, T. F. Heinz, J. Guo, J. Hone, P. Kim, *Nat. Nanotech.* **2014**, *9*, 676.
[30] C. Soci, A. Zhang, B. Xiang, S. A. Dayeh, D. P. R. Aplin, J. Park, X. Y. Bao, Y. H. Lo, D. Wang, *Nano Lett.* **2007**, *7*, 1003.
[31] Y. Zhang, T. Liu, B.o Meng, X. Li, G. Liang, X. Hu, Q.i J. Wang, *Nat. Commun.* **2013**, *4*, 1811.
[32] W. Zhang, J.-K. Huang, C.-H. Chen, Y.-H. Chang, Y.-J. Cheng, L.-J. Li, *Adv. Mater.* **2013**, *25*, 3456.
[33] O. Lopez-Sanchez, D. Lembke, M. Kayci, A. Radenovic, A. Kis, *Nat. Nanotech.* **2013**, *8*, 497.
[34] C.-C. Wu, D. Jariwala, V. K. Sangwan, T. J. Marks, M. C. Hersam, L. J. Lauhon, *J. Phys. Chem. Lett.* **2013**, *4*, 2508.
[35] Y. Wang, H. Wang, S. M. Gali, N. Turetta, Y. Yao, C. Wang, Y. Chen, D. Beljonne, *Adv. Funct. Mater.* **2021**, 2103353.

[36] C. Soci, A. Zhang, B. Xiang, S. A. Dayeh, D. P. R. Aplin, J. Park, X. Y. Bao, Y. H. Lo, D. Wang, *Nano Lett.* **2007**, *7*, 1003.
[37] F. González-Posada, R. Songmuang, M. Den Hertog, *Nano. Lett.* **2012**, *12*, 172.
[38] S. Sett, R. S. Bisht, A. Ghatak, *Appl. Surf. Sci.* **2019**, *497*, 143754.
[39] V. Klee, E. Preciado, D. Barroso, A. E. Nguyen, C. Lee, K. J. Erickson, M. Triplett, B. Davis, I.-H. Lu, S. Bobek, J. Mckinley, J. P. Martinez, J. Mann, A. A. Talin, L. Bartels, *Nano Lett.* **2015**, *15*, 2612.
[40] L. Li, W. Wang, L. Gan, N. Zhou, X. Zhu, Q.i Zhang, H. Li, M. Tian, *Adv. Funct. Mater.* **2016**, *26*, 8281.
[41] H. Schlosser, *J. Appl. Phys.* **1957**, *28*, 512.
[42] S. Mukherjee, T. Maitra, A. Pradhan, S. Mukherjee, S. Bhunia, *Sol. Ener. Mater. Sol. cell.* **2020**, *208*, 110386.
[43] J. A. Peters, N. K. Cho, Z. Liu, B. W. Wessels, H. Li, J. Androulakis, M. G. Kanatzidis, *J. Appl. Phys.* **2012**, *112*, 063702.
[44] A. A. Balandin, *Nat. Nanotech.* **2013**, *8*, 549.
[45] M. Long, Y. Wang, P. Wang, X. Zhou, H. Xia, C. Luo, S. Huang, G. Zhang, H. Yan, Z. Fan, X. Wu, X. Chen, W. Lu, W. Hu, *ACS Nano.* **2019**, *13*, 2511.
[46] M. Long, A. Gao, P. Wang, H. Xia, C. Ott, C. Pan, Y. Fu, E. Liu, X. Chen, W. Lu, T. Nilges, J. Xu, X. Wang, W. Hu, F. Miao, *Sci. Adv.* **2017**, *3*, e1700589.